Subglacial and Underground Structures Detected from Recent Gravito-Topography Data

Subglacial and Underground Structures Detected from Recent Gravito-Topography Data

By

Jaroslav Klokočník, Jan Kostelecký, Václav Cílek and Aleš Bezděk

Cambridge
Scholars
Publishing

Subglacial and Underground Structures Detected from Recent Gravito-Topography Data

By Jaroslav Klokočník, Jan Kostelecký, Václav Cílek and Aleš Bezděk

TABLE OF CONTENTS

ACKNOWLEDGEMENTS

SECTION 1

INTRODUCTION

The shape of the Earth has been studied using various terrestrial, often laborious measurements. Satellite dynamics dealing with perturbations in the motion of the Earth's artificial satellites, arising due to the density irregularities of the Earth's body, provide an elegant tool for much more general, deeper and precise knowledge of its shape and gravity field. The shape of the Earth is only roughly approximated to an ellipsoid (usually a rotational ellipsoid), but more precisely approximated to a *geoid* (an equipotential surface that the *ocean* surface would take under the influence of *gravity* and *rotation* of the *Earth* alone, if other influences were absent). Today we know it with sub-metre precision, on the open oceans and some parts of the continents even to the centimetre level.

To determine a geoid, we use and combine various types of satellite and terrestrial observations. These were observations of satellites from the ground by special cameras and laser radars; but now are mostly observations from satellites down to the ground (satellite altimetry); between two satellites in orbit (satellite-to-satellite tracking); GPS observations and measurements of microaccelerations; and their differences on orbiting spacecraft (space-borne gradiometry).

To describe a geoid, we very often make use of the expansion of the gravitational potential in the spherical harmonic functions (a mathematical tool known from other disciplines). A set of such numbers (harmonic geopotential coefficients or Stokes parameters) is called a gravity (gravitational) model of the Earth (in short: the Earth model). The first gravity field model derived from satellite (camera) observations (Standard Earth SAO, Lundquist and Veis 1966) provided the ground resolution of a few thousand kilometres and the precision of a geoid of tens of metres. Now, with a combination of diverse satellite and terrestrial data and advanced computing techniques, we are at a global ground resolution ~10 km. This yields the space for many applications in geoscience (satellite dynamics

itself, a more precise orbit determination of the next satellites, geodesy, geophysics, geology, oceanology, cryology, morphology…).

This book is about the present-day level of selected results of gravity field research for the geosciences. We will not return to history. We will deal with the recent gravity field model EIGEN 6C4 (Foerste et al. 2014), surface and subglacial topography models and the magnetic field model EMAG 2 (Maus et al. 2009).

It is important to note that we work with gravity aspects (descriptors), as well as with traditional geoid undulations and gravity anomalies. This enables, expands and enriches the possibility of various geo-applications, as the reader will see. This method is novel; it is our contribution to interpreting the gravitational results for the Earth in various geoscience branches.

This book is more or less a summary of our achievements, in a context of the results achieved by others before us, in gravity field applications in geoscience during the last ten years; we have utilized various materials from our previous journal papers and conference presentations.

In Section 2, we outline theoretical preliminaries which the reader needs to know to understand our activities described in this book. We not only provide the necessary formulae, but also comment on their physical meaning and present examples of various gravitational aspects and geological objects from all over the world.

In Section 3, we deal with a description of the input data for our analyses (the gravity data, topography and other data) and explain the term "resolution". It is important to touch upon the problematics of the data coverage and the danger of artefacts arising from insufficient or anisotropic data distribution.

Section 4 is devoted to the subglacial features in Antarctica. We give information about our discoveries of candidates for subglacial volcanoes, lakes, and a lake basin and we contribute to the discussion about the possible impact origin of the near-circular structure in Wilkes Land.

In Section 5, we discuss our results on paleolakes known to geologists in the Sahara, as well as new candidates (the Great Sand Sea in Egypt). We were able to estimate the possible position, extent and shape of a paleolake in this area in conjunction (and in good agreement) with archaeological data about former local settlements.

Section 6 is about impact craters on the Earth that are in some way specific: hidden under the ice (Antarctica, Greenland) or under younger sediments (Chicxulub, Yucatan), sitting on the ocean bottom (Burckle, the Indian Ocean) or an impact event without any crater (Saginaw Bay, the Great Lakes area). There is often effusive disputation about these objects mainly among geologists; it would be boring to present well-known, established, and accepted conclusions; it is better to provoke with new things and ideas (although it can be risky).

In Section 7, we ask whether it is possible to indicate oil and gas deposits (more generally, hydrocarbons, coal, water…) with gravitational aspects, namely with combed strike angles. We test such a hypothesis (from our previous works) on known huge oil/gas mining localities and provide extrapolations to other places. It may be surprising that even the impact craters on the Earth show a relationship to oil-/gas-rich deposits or various economic minerals.

In Section 8 we focus on the variable part of the gravity field; data collected over a period of nearly 15 years are now available from the satellite GRACE mission. Although its resolution is much lower than that of the static part of the gravity field and thus in all previous geo-applications (Sect. 4-7), the results concerning global change are encouraging. Section 9 is the conclusion.

This book only deals with the Earth, but the same methodology is valid and being tested for other celestial bodies where we have already achieved some level of knowledge about their gravitational fields (for example the Moon, Mars or Venus).

SECTION 2

THEORY AND EXAMPLES

2.1. Summary of formulae and comments on their physical meaning

The theory summarized here is repeated from the literature; it is taken mostly from Pedersen and Rasmussen (1990), Beiki and Pedersen (2010) and from our own papers, Kalvoda et al. (2013) and Klokočník et al. (2014, 2016) – and also partly from other sources (for references, see below). It has also been presented (in a shorter and less complete version than here) in our book, Klokočník et al. (2017b). Here we provide all of the needed formulae, comments on their physical meaning (Sects. 2.1 and 2.2), practical use and how they are computed (Sect. 2.3), and we present examples – figures (in Sect. 2.4). In the notation of physical quantities, we often follow Pedersen and Rasmussen (1990).

The *disturbing static global gravitational potential* outside the masses of a celestial body (planets, moons) in the spherical harmonic expansion is given by

$$T(r, \varphi, \lambda) = \frac{GM}{r} \sum_{l=2}^{\infty} \sum_{m=0}^{l} \left(\frac{R}{r}\right)^l \left(C'_{l,m} \cos m\lambda + S_{l,m} \sin m\lambda\right) P_{l,m}(\sin \varphi), \tag{1}$$

where *GM* is a product of the universal gravitational constant *G* and the mass *M* of the planet (also known from satellite analyses as the geocentric gravitational constant in the case of the Earth), *r* is the radial distance of an external point where *T* is computed, *R* is the radius of the Earth (which can be approximated by the semi-major axis of a reference ellipsoid), $P_{l,m}$ *(sin φ)* are the Legendre associated functions, *l* and *m* are the degree and order of the harmonic expansion, (*φ, λ*) are the geocentric latitude and longitude, and $C'_{l,m}$ and $S_{l,m}$ are the *harmonic geopotential coefficients* (also known as *Stokes parameters*); fully normalized, $C'_{l,m} = C_{l,m} - C^{el}_{l,m}$, where $C^{el}_{l,m}$ belongs to the reference ellipsoid. The word "disturbing" here means the difference between the total gravitational potential of the actual body and the gravitational potential of a reference body, i.e. the reference ellipsoid,

usually taken as a rotational ellipsoid with some flattening on the poles due to the rotation of that body.

A set of numbers $C'_{l,m}$ and $S_{l,m}$, presented to a maximum degree L_{max}, is called the *gravity/gravitational field model of the Earth*. There is $l \times (l-1)$ terms in such a model, if is complete to the maximum degree and order l, m (or d/o) and if a few first (lowest degree) terms are not omitted (sometimes these terms are set at zero, due to reasons which will not be discussed here).

The gravity models are usually based on a great amount of diverse satellite and terrestrial data collected from around the world over a long time; then such a result is known as a high-resolution "*combined model*" (e.g., GEM 2008, Pavlis et al. 2012; EIGEN 6C4, Foerste et al. 2014) in contrast to *satellite-only models*.

Let us remember that $C'_{l,m}$ and $S_{l,m}$ are considered to be constants in unvarying gravity field models (excluding a few lowest degree zonal harmonics, which have often published a secular trend and semi/annual or other time variable components). We speak about *static gravity models*.

There are also variable gravity field solutions, derived from global satellite data (mainly from the GRACE mission). They are based on short arc solutions (from observations gathered during one month or a shorter interval), so they are available for a much lower L_{max} than the static models (say to $d/o = \sim100$ instead of ~2000). The variable field will be considered in Section 8.

The *gravity (gravitational) aspect* is a functional/function of the gravity (gravitational) field potential T. It can be its derivative or any other function, often non-linear. We work with the following *gravity aspects* (descriptors): the gravity anomaly (or disturbance) Δg, the Marussi tensor (Γ) of the second derivatives of the disturbing potential (T_{ij}), two gravity invariants (I_j), their specific ratio (I), the strike angles (θ) and the virtual deformations (vd) – Klokočník et al. (2017b).

All the gravity aspects together provide thorough information about the density anomaly due to the causative body. It is more complete than information that the traditional and usual gravity anomalies alone could yield. The set of gravity aspects informs about location, shape, orientation, a tendency to a 2D or 3D pattern, and stress tendencies and may partly simulate "dynamic information" although the input data are always the same – those harmonic geopotential coefficients $C'_{l,m}$ and $S_{l,m}$ of a *static* gravity

field model. The whole theory is arranged in such a way that we cannot use any input other than the harmonic coefficients of a gravity model.

 Now we will define the individual gravity aspects, starting with the traditional gravity anomalies often used in geophysics, geodesy, etc.

 The spherical approximation of the *gravity anomaly Δg* (free air, without any geophysical model) is computed as the first radial derivative of *T* by

$$\Delta g = -\frac{\partial T}{\partial r} - 2\frac{T}{r}. \tag{2}$$

 Instead of (2), one can use the *gravity disturbance*, which is as (2), but without the second term (often small). The gravity anomalies/disturbances are computed from measurements by ground, aeroplane or marine gravimeters or derived from measurements performed by means of satellite altimetry. One example of *Δg* [mGal] is in Fig. 2-2, Sect. 2.4, for the whole Antarctica continent, and there are many more in other chapters.

 The gravity gradient tensor **Γ** (the *Marussi tensor* or simply the *gravity tensor*) is a tensor of the second derivatives of the disturbing potential *T* of the particular gravitational field model (Marussi 1985, originally in the Italian language in 1951; Rummel 1986). The Marussi tensor was considered the centrepiece of traditional differential geodesy; up to the second order this tensor systematically synthesizes all of the dynamical and geometric properties of the Earth's gravity field. The second derivatives are expressed in the local north-oriented reference frame (*x*, *y*, *z*), where *z* has the geocentric radial direction, *x* points to the north and *y* is directed to the west (Pedersen and Rasmussen, 1990):

$$\mathbf{\Gamma} = \begin{bmatrix} T_{xx} & T_{xy} & T_{xz} \\ T_{yx} & T_{yy} & T_{yz} \\ T_{zx} & T_{zy} & T_{zz} \end{bmatrix} = \begin{bmatrix} \frac{\partial^2 V}{\partial x^2} & \frac{\partial^2 V}{\partial x \partial y} & \frac{\partial^2 V}{\partial x \partial z} \\ \frac{\partial^2 V}{\partial y \partial x} & \frac{\partial^2 V}{\partial y^2} & \frac{\partial^2 V}{\partial y \partial z} \\ \frac{\partial^2 V}{\partial z \partial x} & \frac{\partial^2 V}{\partial z \partial y} & \frac{\partial^2 V}{\partial z^2} \end{bmatrix} \tag{3}$$

 Outside of the body masses **Γ** satisfies Laplace's differential equation, i.e. the trace of the Marussi tensor (3) is zero. The tensor **Γ** is symmetric ($T_{yx}=T_{xy}$, $T_{zx}=T_{xz}$, $T_{zy}=T_{yz}$) and harmonic ($T_{xx}+T_{yy}+T_{zz}=0$); it contains nine components, but just five linearly independent components.

 Gravitational gradiometry is the measurements of T_{ij}. Gravimeters measure the first derivative of *T*, i.e. the accelerations *Δg*, and the gradiometers

measure the second derivatives of T. From the actual formulae for their computation one can see that the gravitational gradients are more sensitive to the close-by mass distribution (density anomalies) than the gravitational accelerations. We show this clearly by means of Fig. 2-1 in Sect. 2.3 (and not only for a comparison between the first and second derivatives).

The importance of the second derivatives was recognized by Marussi (1985), Hotine (1969), and Elkins (1951, p. 29) who stated: "…the double differentiation with respect to depth tends to emphasize the smaller, shallower geologic anomalies at the expense of larger, regional features"… and that they provide "…often a clearer and better resolved picture…[more] important in oil or mineral exploration than is the original gravity (anomaly) picture".

Terrestrial gradiometers (torse balances) to measure T_{ij} are known from geophysics (see any geophysics textbook), but they were not too successful in practical use (too noisy). Now, owing to technical progress, they can successfully be used for measurements on board aeroplanes (e.g. Bell Company, 2010) and are used for prospection at local scales.

We recall a few classic works about theoretical/physical geodesy that are useful to read for deeper information than can be provided here (Hotine 1969; Hofmann-Wellenhof and Moritz 2005; Rummel et al. 2011).

Some theoretical works about space gravitational gradiometry and preparation for gravity space missions are also old, now classic, but still valid, see e.g., Balmino et al. (1981), NASA (1984), Rummel (1986), ESA (1999), Baur et al. (2007). There one can find two concepts for space gradiometers: a combination of microaccelerometers (e.g. Balmino et al. 1981) and superconducting gravity gradiometers (e.g. NASA 1988). The *GOCE* mission (Gravity and Ocean Circulation Explorer, ESA) was the first (2009) and until now (2020), still the last gradiometric instrument working successfully in space (measuring six of T_{ij} million times during its 5-year lifetime at a carefully selected low orbit fulfilling special criteria on orbital resonances), based on microaccelerometers (a pair of them in each spatial direction). See more in Sect. 3.2 about the GOCE.

One illustrative example of T_{zz} for Mt Sidley (the largest known volcano in Antarctica, partly visible on the ice surface) for this section is shown in Fig. 2-4a; the full tensor $\mathbf{\Gamma}$ for Lake Vostok (LV) is shown in Section 4, Sect. 4.3.4., Figs. 4-7 a-f, and there are more examples with T_{zz} elsewhere in this book.

The Marussi tensor has already been used locally (this means in areas of a few per few kilometres) for petroleum, metal, diamond, groundwater, etc., explorations (e.g., Zhang et al. 2000, Saad 2006, Murphy 2007, Mataragio and Kieley 2009, Murphy and Dickinson 2009 and others). The full Marussi tensor is a rich source of information about density anomalies providing useful details about the target objects shallowly located beneath the Earth's surface. This extra information can be used by tensor imaging techniques to enhance the source anomalies; it has been tested for local features (economic minerals, oil and gas deposits, fault location, etc.), see e.g. Saad (2006), Murphy and Dickinson (2009) or Mataragio and Kieley (2009). The tensor components are used at local scales to identify and map the geological contact information, either the edges of the source targets or the structural/stratigraphic contact information. The horizontal components identify the shape and the geological setting of a responsible body. The quantity T_{zz} is best suited for target body detection; T_{zz} helps to define the isopath/density relationships of body mass with relation to its geological setting, see e.g. Saad (2006).

The third derivatives T_{ijk} of the disturbing potential T have been studied by Šprlák et al. (2015); there are just seven T_{ijk} rather than five independent components T_{ij} in Γ. The question that arises is their potentiality for practical use (these are inevitably noisy values when computing them with the actual data) and their physical meaning should also be clarified. We tested T_{zzz} for various geological features but we do not work with T_{ijk} here.

Under arbitrary coordinate transformation, any gravity field and any Γ have just three global *gravity invariants* which remain constant (Pedersen and Rasmussen 1990; Rummel 1986; Baur et al. 2007, etc.). Here they are labelled I_0, I_1, and I_2:

$$I_0 = trace\ (\Gamma)$$

and this one is zero outside the masses of the studied body (known also as the Laplace equation). The remaining two invariants read in general:

$$I_1 = \tfrac{1}{2}\ [\text{trace}\ (\Gamma)^2 - \text{trace}\ (\Gamma^2)],$$

$$I_2 = det\ (\Gamma).$$

This can be transformed (using the components of Γ in Eq. 3) to:

$$I_0 = T_{xx} + T_{yy} + T_{zz}$$

$$I_1 = (T_{xx}T_{yy}+T_{yy}T_{zz}+T_{xx}T_{zz}) - (T_{xy}^2+T_{yz}^2+T_{xz}^2) =$$

$$\sum_{\{i,j\}\in\{x,y,z\}}\left(T_{ii}T_{jj} - T_{ij}^2\right) \tag{4}$$

$$= -(T_{xx}^2+T_{yy}^2+T_{xx}T_{yy}+T_{xy}^2+T_{yz}^2+T_{xz}^2),$$

$$I_2 = det\,(\mathbf{\Gamma}) =$$

$$= T_{xx}\,(T_{yy}T_{zz}-T_{yz}^2) + T_{xy}\,(T_{yz}T_{xz}-T_{xy}T_{zz}) + T_{xz}\,(T_{xy}T_{yz}-T_{xz}T_{yy}) \tag{5}$$

The invariants are mathematically independent of the coordinate system chosen, so invariant ("resistant") with respect to any rotation. The invariant I_0 is useful for numerical checks of the actually measured T_{ii}. The invariant I_1 is the sum of the six products of two tensor coefficient matrix elements, a nonlinear functional model with regard to the geopotential harmonics. The invariant I_2 is the determinant "det" of $\mathbf{\Gamma}$.

The invariants can be looked upon as non-linear filters enhancing sources with big volumes (Pedersen and Rasmussen 1990). They discriminate major density anomalies into separate units; examples are in Figs. 2-4b and 2-7c. It is useful and helpful that the resultant computed anomaly response retains the same shape and orientation, i.e. it is independent of the observer's choice of axes; this is significant for interpretation when mapping geological structures.

The invariants were also tested for the inversion from gravimetric measurements to $C'_{l,m}$ and $S_{l,m}$ in (1), see e.g. a pioneer work by Baur et al. (2007 and Baur's thesis before this). The advantage is that the invariants are invariant, not dependent on the orientation errors of the measuring device in space. The disadvantage is their nonlinearity, see Eqs. 4 and 5. It was recognized that they do not bring any new information about the gravity field.

Other combinations of the components of the Marussi tensor are possible. The invariance is also valid for the following two combinations for the horizontal components derived from $\mathbf{\Gamma}$ (Pajot et al. 2004; Murphy 2007). They were applied in geology, e.g., by Murphy and Dickinson (2009):

$$Th = InVar\_TxzTyz = \sqrt{T_{xz}^2 + T_{yz}^2}$$

$$InVar\_TxyTxxTyy = \sqrt{T_{xy}^2 + \left((T_{yy} - T_{xx})/2\right)^2}.$$

We tested the quantity *Th* for various geological structures on the Earth, but we do not use it here. *Th* is also known as the total horizontal derivative (Andrews-Hanna et al. 2012; these authors also defined and used the horizontal curvature of the potential field: $\sqrt{[T_{xx}^2 + T_{yy}^2]}$).

Pedersen and Rasmussen (1990) showed that the ratio *I* of the invariants *I_1* and *I_2,* defined as

$$0 \le I = -\frac{(I_2/2)^2}{(I_1/3)^3} \le 1 \, , \tag{6}$$

always lies between zero and unity for any potential field. If the causative body is strictly 2D, then *I*=0. Thus, the ratio can be an indicator of two-dimensionality, sometimes called the "*2D factor*". If *I*=0, then we have the necessary but not sufficient condition for two-dimensionality. When the causative body as seen from the observation point looks more 3D-like (for example, a volcano), then *I* increases and eventually approaches unity. We have examples in Sect. 2.4.

The gradient tensor **Γ** contains information about subsurface strike (stress) directions. Pedersen and Rasmussen (1990) defined the *strike angle θ* (strike lineaments, strike direction) as follows:

$$\tan 2\theta_s = 2\frac{T_{xy}(T_{xx}+T_{yy})+T_{xz}T_{yz}}{T_{xx}^2-T_{yy}^2+T_{xz}^2-T_{yz}^2} = 2\frac{-T_{xy}T_{zz}+T_{xz}T_{yz}}{T_{xz}^2-T_{yz}^2+ T_{zz}(T_{xx}-T_{yy})} \tag{7}$$

where *θ* is estimated within a multiple of π/2; and only one value represents the main direction of **Γ**. Provided that the ratio *I* in (6) is small, the strike angle may indicate a dominant 2D structure. If one were able to rotate with the structure in such a way that the elements of the first row and first column of **Γ** were identically equal to zero, then one would reach a "correct" direction of "stress fields" described by *θ* (Beiki and Pedersen, 2010, Murphy and Dickinson, 2009).

Mathematically, *θ* is the main direction of **Γ**. Geophysically, it is an important direction for the ground structures; it may indicate areas with a lower porosity or "stress directions".

The strike angles usually have various directions. Sometimes they are oriented dominantly in one direction; we say they are "combed" (Figs. 2-5, 9a, b). The theory of combed θ has been presented for the first time by Klokočník et al. (2019) and it is described below (Sect. 2.2). The combed values, mostly for small I $(I<0.3)$ may predict, among others, possible oil or gas fields. This was discovered by Klokočník and Kostelecký (2015) and is further elaborated in Sect. 7 (Klokočník et al. 2020a).

The situation remains, however, not unambiguous when solely using the gravity data. The reason is that not only can oil and gas fields be detected by the combed θ but also groundwater reservoirs, water-filled depressions, paleolakes or stress fields after impact at and near the impact craters (see also Sects. 2.2, 6, 7). The combed θ probably relates to changes of porosity, for example possibly revealing the porosity increase due to an impact pressure deformation. It is evident that we need additional information to the gravity aspects; this means geological or geophysical information, namely magnetic anomalies, archaeological data, etc.

We have defined six gravity aspects (the gravity anomalies or disturbances, the Marussi tensor, the invariants – two out of three are used, their specific ratio, and the strike angles); each has specific properties, a specific reaction to density anomalies under the surface, although all are derived from one and the same T.

Now we define a new quantity which we call *"virtual deformation"* (*vd*), introduced for the first time by J. Kostelecký in Kalvoda et al. (2013) and Klokočník et al. (2014). It is analogous to the tidal deformation from geodesy and geophysics; one can imagine the directions of such a deformation due to "erosion" brought about solely by gravity.

If there were a tidal potential represented as in our case by T (1), then horizontal shifts (deformations) would exist due to this and they could be expressed in the north-south direction (latitude direction) as

$$u_\Phi = l_S \frac{1}{g} \frac{\partial T}{\partial \varphi} \qquad (8)$$

and in the east-west direction (longitudinal direction) as

$$u_\Lambda = l_S \frac{1}{g cos\ \varphi} \frac{\partial T}{\partial \lambda} \qquad (9)$$

where g is the gravity acceleration 9.81 m·s^{-2}, l_S is the elastic coefficient (called the Shida number) expressing the elastic properties of the Earth as a planet (generally $l_S = 0.08$), φ and λ are the geocentric latitude and longitude of the point P where we measure T; and the potential T is expressed in [m^2 s^{-2}]. In our case, T is represented by Eqs. (1), (8) and (9). The practical problem is that the actual values of the Shida parameters l_S for the Earth's surface (for the specific locations) are not known; thus, we will know (8) and (9) and subsequent quantities only as relative values.

The formalism of continuum mechanics was applied to derive the main directions of the deformations, meaning to transform the horizontal shifts to a small deformation (e.g., Brdička et al. 2000). The tensor of a small deformation E is defined as a gradient of the horizontal shifts (8) and (9):

$$E = \begin{pmatrix} \epsilon_{11} & \epsilon_{12} \\ \epsilon_{21} & \epsilon_{22} \end{pmatrix} = \begin{pmatrix} \dfrac{\partial u_x}{\partial x} & \dfrac{\partial u_x}{\partial y} \\ \dfrac{\partial u_y}{\partial x} & \dfrac{\partial u_y}{\partial y} \end{pmatrix}. \tag{10}$$

The tensor E has two parts: $\mathbf{e}$ is the symmetrical, and $\mathbf{\Omega}$ is the anti-symmetrical part:

$$E = \mathbf{e} + \mathbf{\Omega} = \left(e_{ij} \right) + \left(\Omega_{ij} \right) \tag{11}$$

The symmetrical tensor $\mathbf{e}$ reads:

$$\mathbf{e} = \begin{pmatrix} e_{11} & e_{12} \\ e_{21} & e_{22} \end{pmatrix} = \begin{pmatrix} \epsilon_{11} & (\epsilon_{12} + \epsilon_{21})/2 \\ (\epsilon_{12} + \epsilon_{21})/2 & \epsilon_{22} \end{pmatrix}, \tag{12}$$

the parameters of deformation are:

$\Delta = e_{11} + e_{22}$ total dilatation   (13)
$\gamma_1 = e_{11} - e_{22}$ pure cut
$\gamma_2 = 2e_{12}$ technical cut
$\gamma = (\gamma_1^2 + \gamma_2^2)^{1/2}$ total cut
$a = \frac{1}{2}(\Delta + \gamma)$ major semi-axis of the ellipse of deformation
$b = \frac{1}{2}(\Delta - \gamma)$ minor semi-axis of the ellipse of deformation
$\alpha = \frac{1}{2} \operatorname{atan}(\gamma_2/\gamma_1)$ direction of the main axis of deformation.

Note that different specialists make use of different terminology for the same or similar quantities quoted in (13). We follow the textbook written by Brdička et al. (2000).

The derivatives of the disturbing geopotential obtained originally as the directional values (8), (9) were transformed to small positional deformations, or shifts. But basically, the information content of the Marussi tensor and of *vd* is the same, only exposed in different ways.

To illustrate *vds*, the semi-axes ***a***, ***b*** of the deformation ellipse are computed. As we already know, the local values of l_S are not known, and, in turn, only the main directions of *vds* (and not their amplitudes) can be computed.

It is very interesting that *vds* provide dynamical information, even though they are, as well as all the gravity aspects mentioned here, computed from static gravity models (represented by a set of $C'_{l,m}$ and $S_{l,m}$).

As already mentioned, the *vd* is analogous to the tidal deformation and characterizes the "tensions" (geometrically, compression and dilatation) generated by the causative body (Kalvoda et al. 2013). We can understand the *vd* as a principle axis transformation from the horizontal gradients of the deflections of the vertical (8) and (9). Since the potential is forward-modelled from the topography (at least in the case of the RET 14 model, see below), it is also related to the curvature of topography (Klokočník et al. 2014, p. 93). Examples of *vds* are in Figs. 2-3, 2-4c and 2-7d.

2.2. Theory of combed strike angles

As mentioned above in Sect. 2.1, the *combed strike angles* are strike angles θ oriented roughly in one and the same direction. We will define the combed coefficient *Comb* for θ (Klokočník et al. 2019) as a measure or degree of θ being combed; it is a relative value in the interval $\langle 0,1 \rangle$, where 0 means to be "not combed" (the vectors of θ are in diverse directions) and *1* means to be "combed" (perfectly kempt, the vectors of θ are oriented into one prevailing direction).

These are the input data to the statistics:

$$\theta_i \in \langle -90°, 90° \rangle, i = 1, \dots, n$$

for *n* pixels in the studied area or zone. We compute the main direction of the combed θ as the mean value of θ_i; let us denote it as θ_{Comb}:

$$\theta_{Comb} = \frac{\sum_{i=1}^{n} \theta_i}{n}$$

by choosing the angles θ_i either in the interval $\langle -90°, 0°\rangle$ or in the interval $\langle 0°, 90°\rangle$. We use the following important condition:

$$\forall(|\theta_i - \theta_{Comb}| > 90°): \theta_i = 180° - |\theta_i|$$

which means that even two angles θ_i in opposite directions are counted as one direction. For example: for $\theta_{Comb} = 80°$ and $\theta_i = -80°$, a deviation from the main *Comb* direction is 20°.

Let us define a root mean square value of scatter (variance) of θ_i for n pixels as:

$$rmsv = \sqrt{\frac{\sum_{i=1}^{n}(\theta_i - \theta_{Comb})^2}{n}}$$

Then the required looked-for value of the main *Comb* direction can be defined as

$$Comb = 1 - \frac{rmsv}{90°}$$

As a measure of the degree of θ "being combed", we make use of the relative values of θ_i:

$$\theta_i^{relat} = 1 - \frac{abs(\theta_i - \theta_{Comb})}{90°} \qquad (14)$$

So the *Comb* value is the main local direction of the tested set of θ_i in the given region; the departures of the individual θ_i from *Comb* are plotted in a preselected optimum size of n rectangular pixels in a relative scale; these are the values of (14); if some of θ_i fit in the main direction of *Comb*, then the pixel has the value 1; if not, then the values (14) are in the interval $\langle 0,1\rangle$. This serves as a simple statistical evaluation to compare areas with combed strike angles to those with "non-combed" strike angles.

If *Comb* is smaller than 0.55, we say that θ_i of the given region are "not combed"; if *Comb* >0.65, we say θ_i are "combed". There is a "grey zone" between the two, i.e. *Comb*= 0.55–0.65.

Examples with *Comb* statistics are given in Fig. 2-9b and in Section 7.

2.3 Computation, terminology and plotting

Computations of all of the quantities defined above have been performed first with Hotine (1969) and Holmes et al. (2006). The numerical stability of the higher derivatives to a high harmonic degree is very important. We make use of software developed by Sebera et al. (2013) and Bucha and Janák (2013), and our own software (J. Kostelecky's internal report on software to compute virtual deformations, 2012). Bucha and Janák (2013) provide more details about efforts to arrange numerical stability before 2013. Various gravity field models – not only for the Earth (also for Mars, Venus and the Moon) – were used; here we present the results which are nearly always only for the Earth.

 A note on the term "gravity aspects". It is new. It means a grouping of the static gravity potential T to diverse gravity descriptors defined by (2) to (13). Originally (in 2012), we suggested the name "gravity derivates". Our English colleague suggested the name "gravity aspects" instead. We accepted this although in astronomy (two of the authors of this book are also astronomers) the label "aspect" has an astrological connotation. We have been using the term "gravity aspects" since 2013.

 The input to our computations of gravity aspects is always a set of harmonic geopotential coefficients of a given static gravity field model (see the section about data), nothing else. The outputs are always gravity aspects. These are then plotted individually with non-linear scales to exhibit prominent features that we wish to emphasize. We did not use any filter during these computations.

 We have scanned the whole world with the global static gravity field model EIGEN 6C4 (Foerste et al. 2014). We used the 5 arcmin step in latitude and longitude everywhere. This step corresponds to the resolution of EIGEN 6C4 which is dictated by the spherical harmonic expansion of the gravity model available to degree and order 2190 (for more see Sect. 3). We always use this full resolution, not cut at lower degrees.

 For Antarctica specifically, there is another model, combining gravity and base topography data, known as SatGravRET2014 (in short, RET14, Hirt et al. 2016), also developed to degree and order 2190.

 For the many examples with EIGEN 6C4 or RET14 (or with an older gravity model EGM 2008 in older papers) see Kalvoda et al. 2013; Klokočník et al. 2014, 2016, 2017a, b, c, 2018 a, b, 2019; Eppelbaum et al. 2017 or Mizera et al. 2016.

Gravity disturbances are shown in milliGals [*mGal*], and the second order derivatives are in Eötvös [*E*]. These are not *SI* units (but they are used frequently in geophysics). Let us recall that 1 *mGal* = $10^{-5}\,ms^{-2}$ and 1 $E \equiv 1$ E.U. = 1 Eötvös = $10^{-9}\,s^{-2}$. The invariants have units I_1 [s^{-4}] and I_2 [s^{-6}]. The strike angle θ is expressed in degrees [deg, ^{0}] with respect to the local meridian; its demonstration in red means its direction to the east and in blue its direction to the west of the meridian. Sometimes the *Comb* statistics are added. The virtual deformations (*vd*) [-], no scale, are shown in blue, where compression takes place, and in red where dilatation occurs.

To illustrate in a simple example, how the various gravity aspects behave (decrease) with increasing distance from the causative body (in fact a density anomaly), it is assumed that the source body is a mass point, with a selected value of *GM* (for its definition see Eq. 1).

It is obvious from the theory that in this simplified case, with arbitrary *GM=Gm* for a sphere, some aspects do not exist or equal zero. The remaining aspects are shown in Fig. 2-1; here their simplification leads to the invariants $I_1 = -3\ (Gm)^2\,r^{-6}$ and $I_2 = -2\ (Gm)^3\,r^{-9}$.

A diverse speed of decrease of the "gravitational signal" can be seen with the increasing depth of the source mass body for various aspects. The slowest decrease turns out for the gravity anomaly (with r^2). The invariants decrease quickly (with r^6 and r^9).
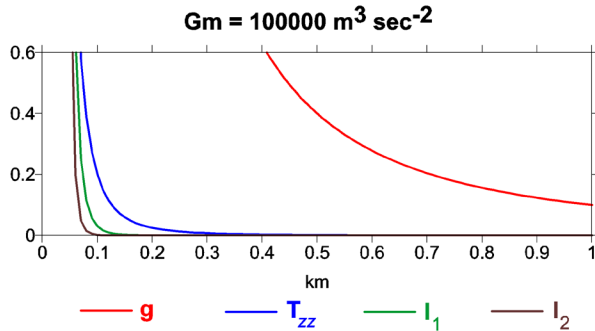
Fig. 2-1. An example of a decrease in the values of the gravity aspects of the model potential with increasing distance (depth) from the source. On the *x* axis there are depths in kilometres, on the *y* axis there is an arbitrary quantity (for a simple intercomparison). This is an illustrative case for a mass point with a randomly selected value of *GM* (here *Gm*, representing a spherical density anomaly)

Fig. 2-1 tells us that aspect I_1 or I_2 best describes the density anomaly in shallow depths under the surface while Δg and T_{zz} are also related to deeper structures. While all of these aspects have the same "common mother" (a recent gravity field model in terms of Stokes parameters), they have different properties (behaviour, sensitivity, relationship to various effective depths of the causative body) and describe the same density anomaly from different views. Thus, their entire set provides much more information, and more complex, but more complete information about the density anomalies (owing to a causative body, target deposits…) than only the traditional Δg could provide. This is the crucial reason to use them all together. Now they do not belong to the "mainstream of geophysics". Not yet. We forecast that they will become a standard in the future.

2.4. Examples

Here we plot a few examples of various gravity aspects to document the theory in Sects. 2.1–2.2. But many more results ordered in a systematic manner can be found in further sections for subglacial volcanoes, lakes and the impact structure in Antarctica, for paleolakes in the Sahara, impact craters and oil and gas deposits, and in our previously published papers mentioned above, for diverse places and geological features in the whole world.

A global view of Antarctica is shown in Fig. 2-2 with Δg, and in Fig. 2-3 using vd. We clearly see well-known mountain belts like the Gamburtsev Subglacial Mountains, valleys, huge subglacial lakes like Lake Vostok (LV), the Wilkes lowland (WL), the Ross Ice Shelf, various iceberg flows, and many others. This is here only to introduce our gravity aspects – we do not interpret these figures.

Mt Sidley is the largest volcano in Antarctica (it is inactive), located in West Antarctica in the Executive Committee Range. Figs. 2-4a, b, and c are intended to show some details for this place in T_{zz}, I_2 and vd. What we can see is the typical gravity signal for any (large) volcano or mountain on the Earth.

We have learnt what is typical of a volcano from many samples of known volcanoes around the world, so later we can extrapolate for subglacial volcano candidates hidden under the ice cover in Antarctica (Section 4), revealing an analogical signal in the form of gravity aspects:

(i)   there is typically a large positive Δg and T_{zz} inside the volcano with a negative belt of T_{zz} around it, exactly according to the theory,

(ii)   the extrema for I_2 (as well as I_1, here always negative) directly over the calderas,

(iii) positive values of vd (dilatation, shown in red) over the volcano with a belt of negative vd around it (compression, in blue),

(iv)   the ratio I is large ($\rightarrow 1$) and the value θ has a tendency to encircle the volcano; for small I, the places in the figures showing θ for volcanoes are (logically) empty (no flat place there).
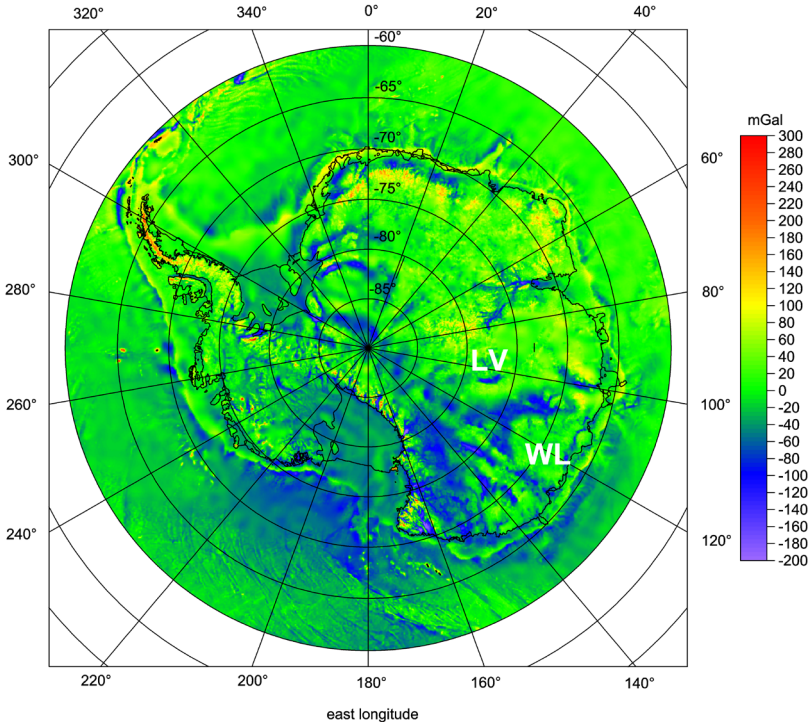

Fig. 2-2. The values of gravity disturbances Δg [mGal] for the whole of Antarctica. The Lake Vostok (LV) is the narrow negative anomaly area at longitudes of about 101–108^{0}E and geodetic latitudes of 76–78^{0}S. The Wilkes Land (WL) anomaly (between longitudes ~100 and 130^{0}E, geodetic latitudes 60^0 and 75^{0}S) is clearly visible as a semi-circular feature with a positive anomaly at its centre and flanking a negative semi-ring anomaly around it
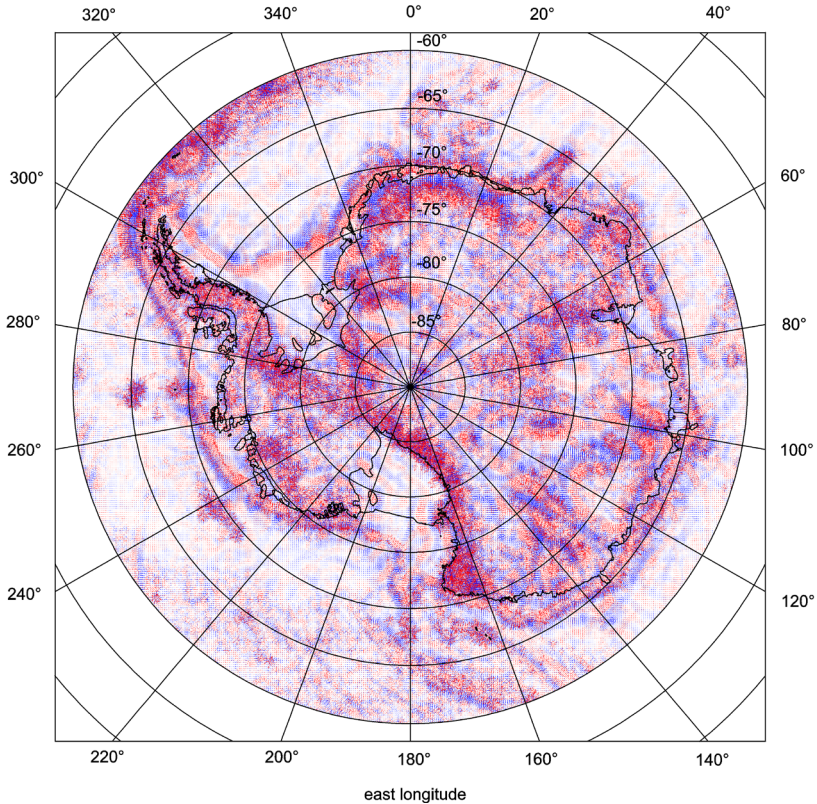
Fig. 2-3. The values of the virtual deformations *vd* [-] (blue for compression, red for dilatation; in fact, these are small arrows plotted at a regular distance and of the same length) for the whole of Antarctica. Compression at LV is surrounded by dilatation. Compression and dilatation zones at WL have a semi-circular shape

As an inspiration for the study of subglacial features in Antarctica, let us point out one of the geological and geomorphological features that is less detectable by other methods than through gravity aspects: the outer margin of the Antarctic Peninsula and the Ross Sea shelves at approximately 200°E. The shelves are depressed to the unusual depth of 500 m due to glacial erosion and isostatic downwarping. The previous sonar and seismic mapping discovered drumlinised relief, end moraines located close to the outer shelf margin and deep troughs downcut by ice streams. The large parts of the shelf areas were covered by a continental glacier. The positive gravity anomalies at the outer margin indicate the existence of moraines and thus

we may guess that the shelves had been part of the glaciated mainland. The negative gravity anomalies oriented perpendicularly, on the other hand, represent troughs formed by ice streams. The zone of particular interest is located between 190° and 210° where the negative zones continue into the shelf margin and deep sea suggesting the existence of wide and possibly shallow troughs of considerable age. This could be the area with the oldest glacial features of the whole continent that were not erased by younger glacial episodes. Other phenomena, such as subglacial volcanoes and lacustrine bases will be described in Section 4.
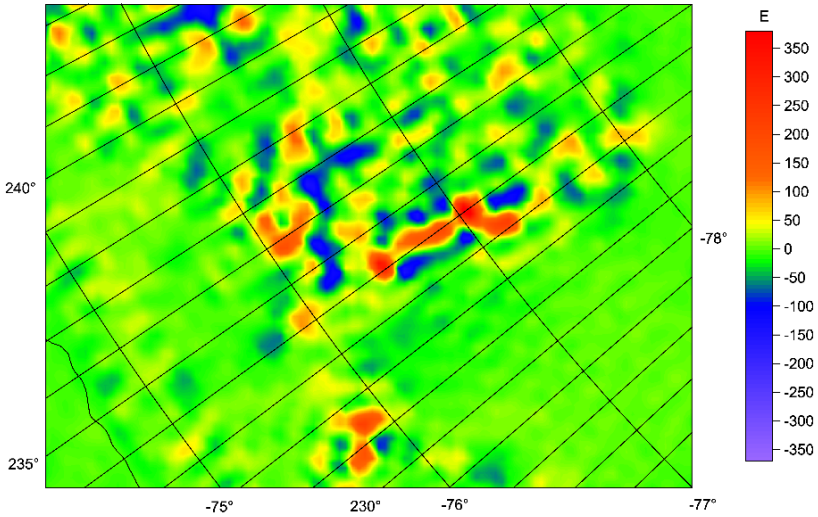
Fig. 2-4a. The Executive Committee Range with the volcano Mt Sidley, West Antarctica, the values of T_{zz} [E]

Figs. 2-4a-c. The gravity aspects with RET 14 for Mt Sidley, visible on the surface, penetrating through the ice, at geodetic latitude $\varphi = 77^0 03'41"$S, longitude $\lambda = 233^0 49'52"$E) and the Executive Committee Range area (the belt with volcanoes in the north-south direction), West Antarctica. North is not up, but along the arrow, in figure **(c)**
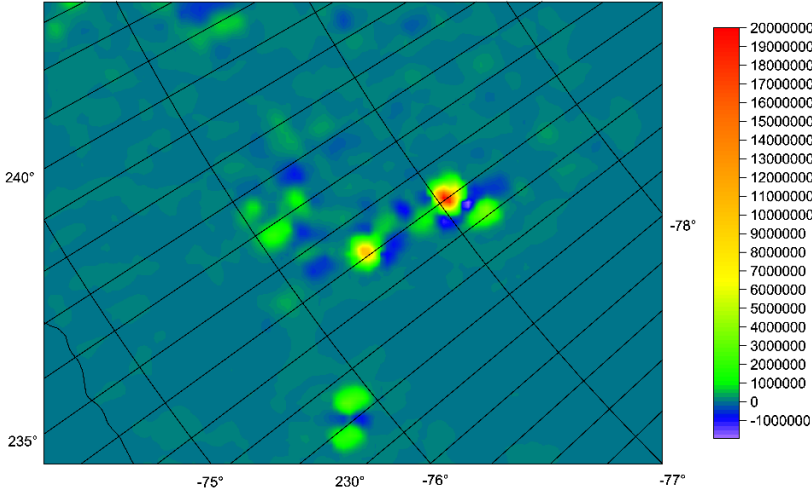
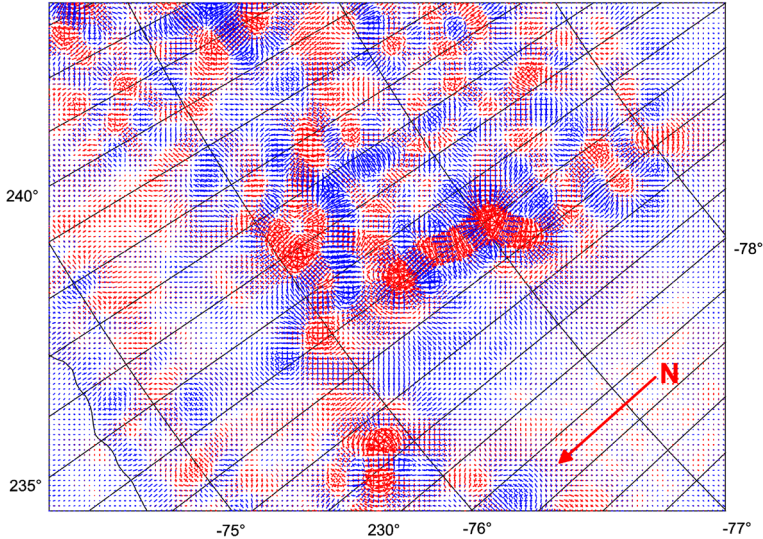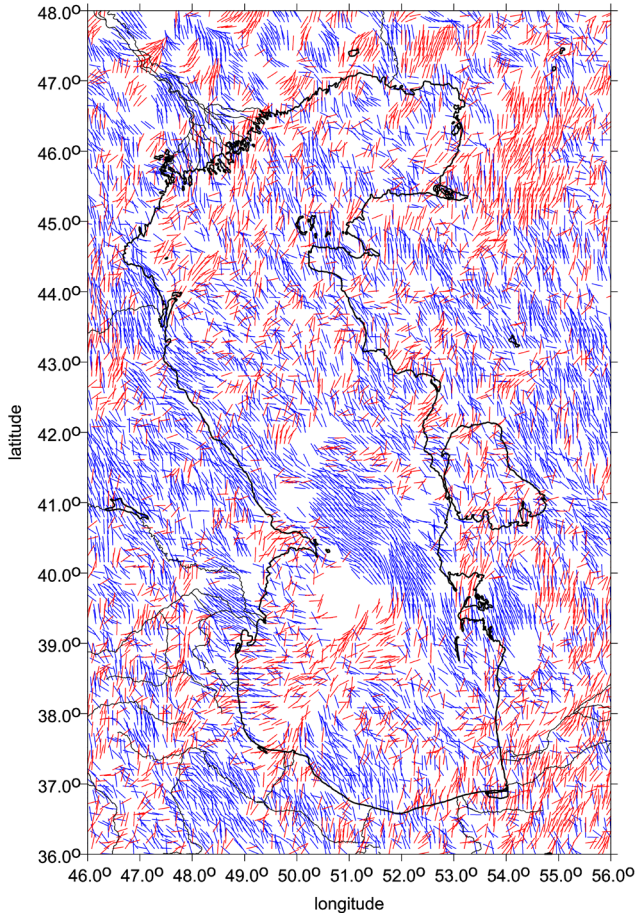**Fig. 2-4b.** I_2 [s^{-4}]

Fig. 2-4c. [vd]

Fig. 2-5. The strike angle θ [deg] in the Caspian sea area with EIGEN 6C4 selected for $I < 0.3$; the large areas with conspicuously one-directionally oriented ("combed") strike angles coincide with the large and known hydrocarbon deposits of the Apsheron Threshold (the lower third of the Caspian Basin) – but θ, as all gravity aspects, is not unambiguous (the areas with combed θ may also be related to (ground) water, a paleolake or oil and gas and water together or nearby impact craters; see the text)

The trench (subduction zone) east of Japan is shown in Fig. 2-6 using virtual deformations *vd*. Note the volcanoes on the ocean bottom, with a typical signal for a volcano: dilatation at its centre, compression around it.
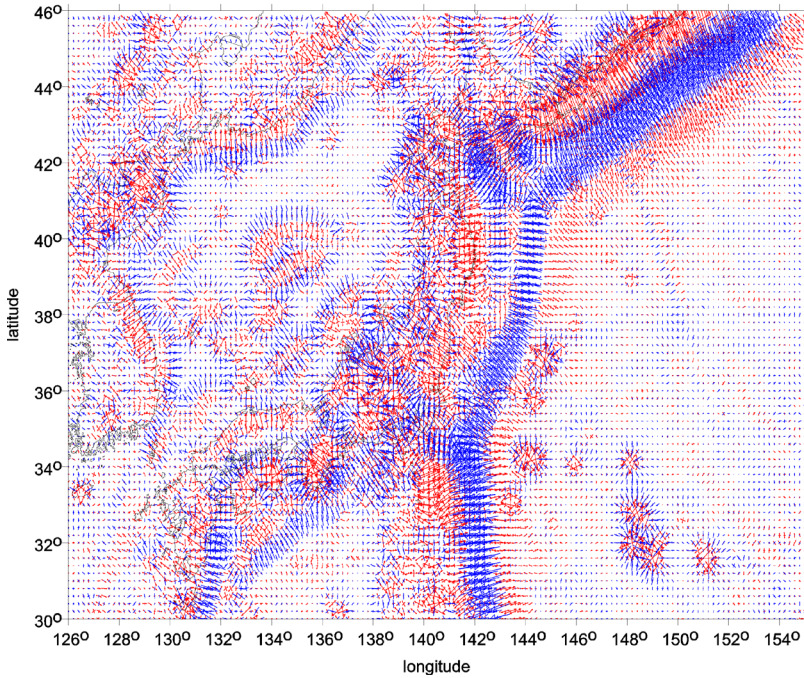
Fig. 2-6. Virtual deformations *vd* [-] computed for Japan and part of the Pacific Ocean with EIGEN 6C4 (zones of dilatations are in red, compressions in blue, in the trench). Note the volcanoes on the ocean bottom

It can be instructive to compare various gravity aspects for the same object. Examples follow for the volcanoes on the Big Island of Hawaii, Figs. 2-7 a, b, c, d for Δg, T_{zz}, I_2 and *vd*, respectively. The second radial derivatives of T_{zz} provide much more detail than Δg, they also form a negative belt around the island; I_2 has extrema values just above the calderas and the *vd* shows dilatation in the volcanoes, while compression frames the island.

a

b